

# Pseudopotential calculations of strained-GeSn/SiGeSn hetero-structures

Saurabh Sant<sup>1, a)</sup> and Andreas Schenk<sup>1</sup>

*Integrated Systems Laboratory, ETH Zurich, CH-8092 Zurich, Switzerland*

We have obtained empirical pseudopotential parameters for  $\alpha$ -Sn and employed the pseudopotential method along with the virtual crystal approximation to model GeSn and SiGeSn alloys. The calculated direct and indirect band gaps of GeSn and SiGeSn show good agreement with experimental data at 300K available till date. The derived pseudopotential parameter set was used to extract various band structure quantities required to model band-to-band tunneling in simulating GeSn/SiGeSn hetero-junction Tunnel Field Effect Transistors (TFET). All the required band structure quantities have been extracted as a function of biaxial strain, Si content, and Sn content and have been fitted to a quadratic expression. An attempt to simulate Si<sub>0.5</sub>Ge<sub>0.5</sub>/Si hetero-junction TFETs based on the extracted band structure quantities yields I<sub>D</sub>-V<sub>G</sub> plots that are in good agreement with the experimental ones - an indication for the reliability of the extracted band structure quantities. Thus, the calculated pseudopotential and extracted band structure parameters provide a complete data base for the modeling of GeSn/SiGeSn hetero-junction TFETs.

Keywords: GeSn, SiGeSn, band structure, empirical pseudopotential method, hetero-junction tunnel FET

GermaniumTin (GeSn) alloys have recently attracted attention due to their capability to achieve direct band gap for certain compositions<sup>1,2</sup> allowing their use in optoelectronic applications<sup>3</sup>. Additionally, the small direct gap of these materials significantly enhances band-to-band tunneling (BTBT) in the presence of an external electric field. This makes them a candidate for Tunnel Field Effect Transistors (TFETs) which are based on BTBT in semiconductors and which are considered as low-power alternatives for Metal-Oxide-Semiconductor Field Effect Transistors (MOSFET)<sup>4</sup>. However, the use of narrow gap materials in the channel and drain region gives rise to ambipolarity in TFETs. This drawback can be overcome by a wide band gap material such as SiGeSn for these parts of the device<sup>5</sup>. Thus, the GeSn/SiGeSn alloy system is suitable for hetero-junction TFETs. Moreover, the GeSn/SiGeSn hetero structure exhibits tunable conduction and valence band offsets which can be useful for waveguide-based optoelectronic applications<sup>3</sup>. In principle, there are three degrees of freedom in selecting the optimum alloy compositions for any of the aforementioned applications, viz, Sn content in GeSn, Si content and Sn content in SiGeSn. The optimal compositions need to be determined by device simulations which require reliable values of the band structure quantities such as direct and indirect band gaps, band offsets, effective masses, etc. In this letter, we present the results of band structure calculations of strained-GeSn and relaxed SiGeSn alloys using the nonlocal Empirical Pseudopotential Method (EPM) which show good agreement with experimental data at 300K. The reliability of the EPM calculations has been asserted by comparing experimental device characteristics of a SiGe/Si hetero-junction nanowire TFET with the simulated characteristics in which the band structure quantities were obtained from the EPM calculations.

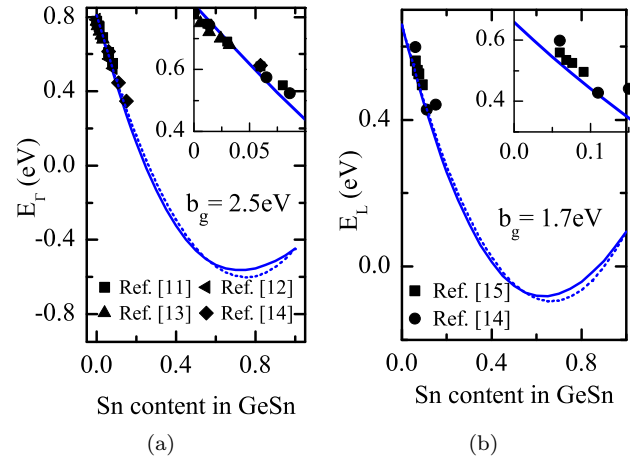


FIG. 1. Comparison of experimental and calculated values of (a) direct band gap in GeSn (magnified view in the inset), (b) indirect band gap in GeSn (magnified view in the inset). The solid line plots the results of pseudopotential calculations while the dotted line plots the bowing expression given by Eq. (1).

The nonlocal EPM parameters used for the band structure calculations are shown in Table I. The nonlocal corrections and the spin-orbit coupling were included in the band structure calculations along with the local pseudopotentials. Pseudopotential parameters of Sn were extracted with S-Band<sup>6</sup> by fitting the calculated band energies at symmetry points to the experimental data. The values of the local pseudopotential at  $|\mathbf{q}|^2 = (3.0, 8.0, 11.0) * (\frac{2\pi}{a_0})^2$  were obtained from the fitting and were interpolated using spline interpolation for intermediate values of the reciprocal vector  $\mathbf{q}$ . A comparison of the calculated and experimental band energies and effective mass values is given in Table II. The energies calculated in this work are similar to those given in Ref. 7. The calculated energies associated with the direct and indirect band gaps ( $\Gamma_{7c}$  and  $L_{6c1}$ ) agree well with

<sup>a)</sup>Electronic mail: sasant@iis.ee.ethz.ch

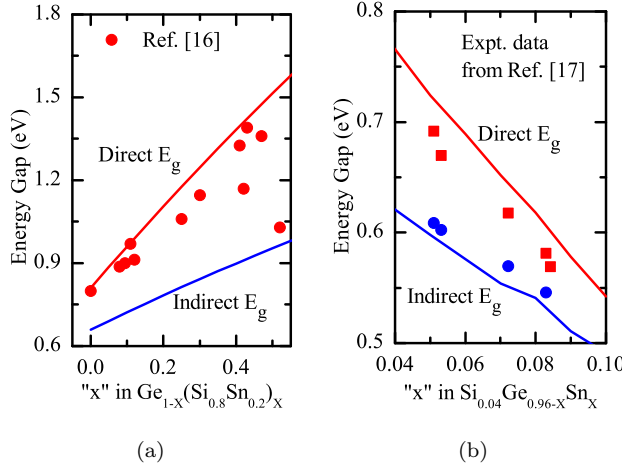


FIG. 2. Comparison of experimental and calculated values of (a) direct and indirect band gaps in  $\text{Ge}_{1-x}(\text{Si}_{0.8}\text{Sn}_{0.2})_x$ , and (b) direct and indirect band gaps in  $\text{Si}_{0.04}\text{Ge}_{0.96-x}\text{Sn}_x$ .

TABLE I. EPM parameter values for Si, Ge and Sn. The parameter values of Si and Ge are taken from Ref. 8

Parameter	Unit	Si	Ge	Sn
$V_{loc}(\sqrt{3})$	Ry	-0.2307	-0.2378	-0.21
$V_{loc}(\sqrt{8})$	Ry	0.0518	0.02852	0.02359
$V_{loc}(\sqrt{11})$	Ry	0.06878	0.0469	0.01737
$\alpha_0$	Ry	0.02815	0.0	0.0
$\beta_0$	1	0.0	0.0	0.365
$R_0$	Å	1.0599	0.0	1.0
$\alpha_2$	Ry	0.0	0.309	0.71
$R_2$	Å	0.0	1.2788	1.453
$\mu$	Ry	0.00018	0.000965	0.00239
$\zeta$	$\frac{1}{(\frac{2\pi}{a_0})^2}$	4.6	5.34	3.97
$q^2$ cutoff	$(\frac{r_{\text{Bohr}}}{a_0})^2$	11.5	12.44	15.25
nonLocalWell	Square	Square	Square	Square

the experimental data. The spin-orbit splitting calculated in this work is smaller than the experimental value. The band structures of GeSn and SiGeSn were calculated by employing the Virtual Crystal Approximation (VCA). The local pseudopotential parameters of the alloy of any given composition were obtained by linearly interpolating the local pseudopotential parameters of the individual atoms. The parameters for Si and Ge were taken from Ref. 8. The variation of lattice constants of GeSn and SiGeSn with the alloy composition was modeled using quadratic expressions fitted to the experimental lattice constants<sup>9</sup>.

The calculated direct and indirect band energies for GeSn are shown in Figs. 1(a) and 1(b), respectively. They are in excellent agreement with the experimental values at 300K. The experimental values of the indirect band gap of GeSn have been extracted at 10K in Ref. 15. Here,

TABLE II. Comparison of the band energies at symmetry points calculated by EPM with the experimental band energies<sup>10</sup> as well as the band energies calculated in Ref. 7. The energies are calculated relative to the valence band edge ( $\Gamma_{8c,v}$ ) of Sn.

Symmetry point	Units	This work	Ref. 7	Exp. <sup>10</sup>
$\Gamma_{6c}$	eV	1.83	2.15	–
$\Gamma_{8c,v}$	eV	0.0	0.0	0.0
$\Gamma_{7c}(E_g)$	eV	-0.448	-0.41	-0.42
$\Gamma_{6v}(\text{SO})$	eV	-0.66	-0.8	-0.8
$L_{6c1}$	eV	0.096	1.4	0.094
$L_{6c2}$	eV	3.22	3.48	–
$L_{4,5v}$	eV	-1.34	-1.2	–
$L_{6v}$	eV	-1.75	-1.68	–
$X_{5c}$	eV	1.04	0.9	–
$m_{\text{LH}}\langle 100 \rangle$	$m_0$	0.04	–	–
$m_{\text{HH}}\langle 100 \rangle$	$m_0$	-0.151	–	-0.19

they are interpolated to 300K by using Varshni's law for the temperature dependence of the indirect band gap<sup>18</sup>. The values of  $\alpha$  and  $\beta$  for elemental Ge are used for the interpolation. Fitting the expression in Eq. (1) to the direct band gap calculated by EPM gives us  $b_g^{\text{Dir}} = 2.5$  eV which is consistent with the previously reported experimental values - 1.94 eV<sup>19</sup>, 2.3 eV<sup>20</sup>, and 2.42 eV<sup>21</sup>. The same fitting procedure yields  $b_g^{\text{Indir}} = 1.7$  eV for indirect band gap calculated by EPM. The calculations suggest that the indirect-to-direct crossover of the band gaps of GeSn alloy occurs at a Sn content of  $\approx 10\%$ . A zero band gap of the GeSn alloy is found at the Sn content of  $\approx 25\%$ . The direct and indirect band gaps of  $(\text{Si}_{0.8}\text{Sn}_{0.2})_x\text{Ge}_{1-x}$  are plotted vs.  $x$  in Fig. 2(a) along with the experimental data. The experimental band gap values are somewhat scattered at intermediate  $x$ . With the exception of a couple of data points, the experimental data show reasonable agreement with the calculations. A comparison between the experimental and calculated band gap values in  $\text{Si}_{0.04}\text{Ge}_{0.96-x}\text{Sn}_x$  shows fair agreement between the two (see Fig. 2(b)). A constant offset of unknown origin is present between the experimental and calculated values of the direct band gap in  $\text{Si}_{0.04}\text{Ge}_{0.96-x}\text{Sn}_x$ .

$$E_g^{\text{Ge}_{1-x}\text{Sn}_x}(x) = x \cdot E_g^{\text{Sn}} + (1-x) \cdot E_g^{\text{Ge}} - b_g \cdot x \cdot (1-x) \quad (1)$$

It is interesting to note that a good reproduction of the experimental data is achieved *without* employing bowing of the EPM parameters. This markedly differs from the previous work on the pseudopotential calculations of GeSn by Gupta *et. al.*<sup>1</sup> in which the authors used nonlinear interpolation of local pseudopotentials to reproduce bowing of the energy gap in GeSn. This difference seems to arise from the shape of the local pseudopotentials used in the two works which are plotted in Fig. 3 versus the magnitude of normalized reciprocal vector. The pseudopotential employed in Ref. 1 spans over only the first nearest neighbour while that used in this work spans over

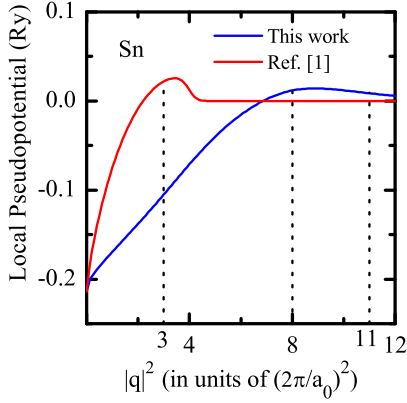


FIG. 3. Comparison of the local pseudopotential of Sn used in this work with that used in Ref. 1. The square of the distances of the first three nearest neighbours in reciprocal lattice space of a diamond crystal are marked by dotted vertical lines.

the first three nearest neighbours. The local pseudopotentials for Ge used in the two works show the same difference as for Sn. This difference in the choice of local pseudopotentials results in significant bowing of the band gap of GeSn in our calculations and its absence in the calculations reported in Ref. 1. The ab-initio Density Functional Theory (DFT) band structure calculations of GeSn reported in Ref. 22 also resulted in a strong bowing of both the direct and indirect band gap when the conventional VCA is employed. This further confirms that by a proper choice of the pseudopotentials it is possible to obtain the bowing of the band gap without introducing nonlinear interpolation of the EPM parameters.

The derived pseudopotential parameter set was used to extract the band-structure quantities required to model BTBT in these semiconductors. The Kane model<sup>29</sup> of BTBT requires the direct band gap, the minima of the  $\Delta$ - and L-valley indirect band gaps, the effective masses in the respective valleys along with the Light Hole (LH) effective mass. The heavy hole bands are usually negligible for BTBT. Therefore, the effective direct tunnel gap can be different from  $E_g$ , but equal to the difference between the energies of  $\Gamma$ -valley Conduction Band (CB) and LH band ( $E_{\text{Tun}}^{\Gamma} = E_{\text{CB}}^{\Gamma} - E_{\text{LH}}^{\Gamma}$ ). This becomes relevant if the LH band falls below the Heavy Hole (HH) band in energy, such as in the case of strain. Since the GeSn active layer with a certain composition is pseudomorphically grown over a GeSn buffer layer, biaxial strain is generated in the active layer. This strain can be used as an additional mean of altering the material band structure. The variation of the band gap in GeSn with Sn content and strain is shown in Fig. 4(a). The LH band is the Valence Band (VB) maximum in the left half whereas the HH band is the VB maximum in the right half. The inclined dashed line in the picture separates the regions where GeSn exhibits direct and indirect band gaps. It is seen that for any strain the band gap becomes direct for large Sn content and that an increasing

TABLE III. The coefficients  $a_1$  to  $a_6$  in Eq. (2) fitted to different band structure quantities in GeSn. The variable  $x_1$  in Eq. (2) represents biaxial strain in the GeSn layer while  $x_2$  in Eq. (2) is the Sn content in GeSn. The values of the band structure quantities at  $0.0 < x_{\text{Sn}} < 0.12$  and  $-0.025 < \epsilon_{\text{GeSn}} < 0.025$  have been included in regression analysis.

Legends	$a_1$	$a_2$	$a_3$	$a_4$	$a_5$	$a_6$
Band energies (eV)						
$E_{\text{CB}}^{\Gamma} - E_{\text{LH}}^{\Gamma}$	0.81	-3.97	-4.0	11.7	-57.3	2.88
$E_{\text{CB}}^{\text{L}} - E_{\text{CB}}^{\Gamma}$	-0.15	5.23	1.696	-6.7	-30.9	-1.41
$E_{\text{HH}}^{\Gamma} - E_{\text{LH}}^{\Gamma}$	0	8.5	0.02	2.99	79.41	-0.336
$\Delta E_{\text{LH}}^{\Gamma}(\text{Strain})$	0	-5.06	-0.034	-5.15	36.5	0.266
Effective masses ( $m_0$ )						
$m_{\text{c}}^{\Gamma}\langle 100 \rangle$	0.042	-0.19	-0.21	0.9	-1.08	0.29
$m_{\text{e},\text{l}}^{\text{L}}$	1.646	-0.76	0.289	-0.496	-104.5	-0.187
$m_{\text{e},\text{t}}^{\text{L}}$	0.091	-0.305	-0.056	0.61	0.775	0.029
$m_{\text{LH}}^{\Gamma}\langle 100 \rangle^{\text{a}}$	0.064	-0.071	-0.226	-1.75	-6.73	-0.342
$m_{\text{HH}}^{\Gamma}\langle 100 \rangle^{\text{a}}$	0.126	1.911	-0.3456	-16.135	-28.1	-1.019

<sup>a</sup> The plots of the LH and HH effective masses vs. strain show spike-like behavior near zero strain<sup>24</sup> ( $-0.02 < \epsilon_{\text{GeSn}} < 0.02$ ). Therefore, the LH and HH masses at zero strain are not included in their respective regression analyses. It is advisable to use the LH and HH masses obtained using the regression coefficients in Table IV in the case of relaxed GeSn.

tensile strain reduces the direct band gap. However, tensile strain also lowers the LH band in energy. As a result, the strain dependence of the effective direct tunnel gap is relatively weak as demonstrated in Fig. 4(b). Hence, the strain in the active GeSn layer might not significantly change the performance of the TFETs. Indirect BTBT is disregarded here as quantum transport simulations have revealed that direct tunneling dominates in small direct-gap semiconductors<sup>23</sup>. All the required band energies and effective mass values in GeSn have been fitted to a quadratic polynomial of the form

$$y = a_1 + a_2 \cdot \epsilon_{\text{GeSn}} + a_3 \cdot x_{\text{Sn}} + a_4 \cdot \epsilon_{\text{GeSn}} \cdot \epsilon_{\text{GeSn}} + a_5 \cdot x_{\text{Sn}} \cdot x_{\text{Sn}} + a_6 \cdot \epsilon_{\text{GeSn}} \cdot x_{\text{Sn}} \quad (2)$$

where  $y$  is the required quantity,  $x_{\text{Sn}}$  is the Sn mole fraction in GeSn and  $\epsilon_{\text{GeSn}}$  is the biaxial strain in GeSn layer given by

$$\epsilon_{\text{GeSn}} = \frac{a_{\parallel}^{\text{GeSn}} - a_0^{\text{GeSn}}}{a_0^{\text{GeSn}}}. \quad (3)$$

The coefficients  $a_1$  to  $a_6$  are listed in Table III for all the required band structure quantities. The band energy “ $E_{\text{LH}}^{\Gamma}(\text{Strain})$ ” in the table refers to the energy level of the LH band in strained GeSn for a given Sn content with respect to its energy level in relaxed GeSn for the same Sn content. This information can be used to obtain the band offsets which will be explained below.

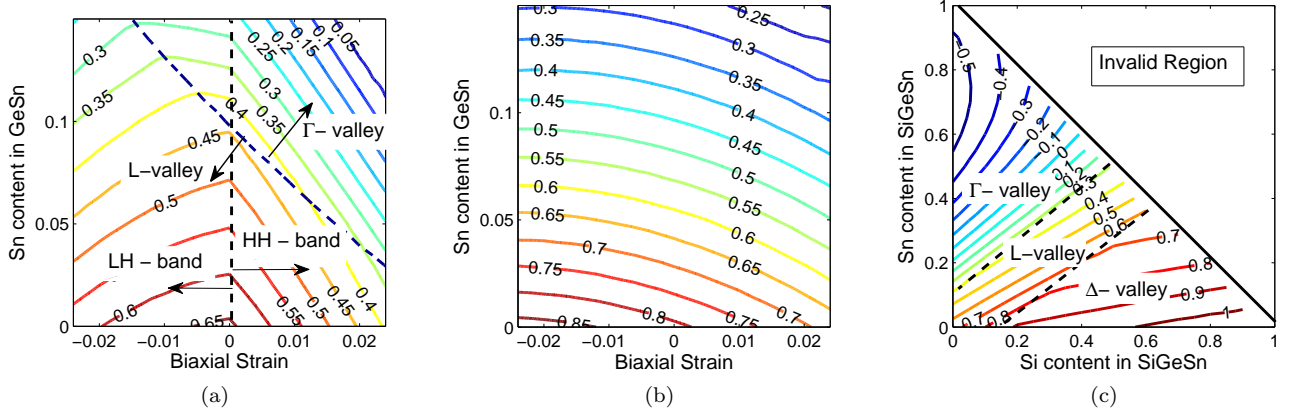


FIG. 4. Contour diagrams showing the variation of (a) band gap (b) effective direct tunnel gap in GeSn with Sn content and strain. The diagrams suggest that the effective direct tunnel gap will be less sensitive to the strain in the GeSn layer. (c) Variation of SiGeSn band gap with Si and Sn content.

TABLE IV. The coefficients  $a_1$  to  $a_6$  in Eq. (2) fitted to different band structure quantities in relaxed SiGeSn. In this case,  $x_1$  in Eq. (2) represents the Si content while  $x_2$  in Eq. (2) is the Sn content in SiGeSn.

Legends	$a_1$	$a_2$	$a_3$	$a_4$	$a_5$	$a_6$
Band energies (eV)						
$E_g^\Gamma$	0.79	3.13	-4.07	-2.85	-0.14	2.96
$E_g^L$	0.659	1.41	-2.39	-1.378	0.041	1.92
$E_g^\Delta$	0.86	0.238	-1.19	-0.479	0.0127	1.26
Effective masses ( $m_0$ )						
$m_e^\Gamma\langle 100 \rangle^a$	0.04	0.112	-0.123	-0.336	0.042	0.284
$m_{e,l}^L$	1.645	-0.051	0.278	-0.046	0.05	-0.074
$m_{e,t}^L$	0.0905	0.037	-0.058	-0.034	0.0	0.049
$m_{LH}^\Gamma\langle 100 \rangle$	0.0526	0.159	-0.237	-0.041	-0.024	0.107
$m_{HH}^\Gamma\langle 100 \rangle$	0.216	0.034	-0.178	-0.069	0.019	0.142

<sup>a</sup> The values of  $m_e^\Gamma\langle 100 \rangle$  for  $E_g < 0.0$  and for  $x_{Si} > 0.9$  have been ignored in the regression analysis.

SiGeSn may be used as a channel and drain material for GeSn/SiGeSn hetero-junction TFETs to reduce ambipolarity and improve TFET performance. Simulation of hetero-junction TFETs requires the band structure quantities of SiGeSn. The EPM was used to calculate these quantities. Relaxed SiGeSn was assumed in the calculations. The variation of the band gap of SiGeSn with Si and Sn content is shown in Fig. 4(c). The contour diagram reveals three distinct regions depending on the position of the conduction band minimum. The CB minimum lies in the  $\Delta$ -valley for large Si content, in the  $\Gamma$ -valley for large Sn content and in the L-valley for intermediate values. For larger Sn content, the alloy becomes metallic (negative direct band gap). Since SiGeSn is relaxed, LH and HH bands are degenerate. Hence, the effective direct and indirect tunnel gaps are equal to the direct and indirect band gaps, respectively. The band

gaps of the  $\Gamma$ -, L- and  $\Delta$ -valley minima as well as the effective mass values were fitted to the quadratic polynomial in Eq. (4).

$$y = a_1 + a_2 \cdot x_{Si} + a_3 \cdot x_{Sn} + a_4 \cdot x_{Si} \cdot x_{Sn} + a_5 \cdot x_{Sn} \cdot x_{Sn} + a_6 \cdot x_{Si} \cdot x_{Sn} \quad (4)$$

Here,  $x_{Si}$  is the Si content in SiGeSn and  $x_{Sn}$  is the Sn content in SiGeSn. The values of the fitted coefficients for each band and effective mass are listed in Table IV.

In addition to the band structure quantities provided above, the band alignment at the GeSn/SiGeSn hetero-junction is also required to model a GeSn/SiGeSn TFET. The energy difference between the VB edges of relaxed GeSn and relaxed SiGeSn can be calculated by employing the expressions given in Ref. 25 that use Jaros' analytical model<sup>26</sup>. This energy difference can be approximated as a VB-offset at the GeSn/SiGeSn interface, given that both layers are fully relaxed ( $E_{V\text{Offset}}^{r\text{-GeSn}/r\text{-SiGeSn}}$ ). The compressive (tensile) strain pushes the LH (HH) band above its energy in the relaxed layer. This effect must be added to the relaxed VB-offset to obtain the strained VB-offset. The strained VB-offset between s-GeSn and r-SiGeSn can be calculated as follows,

$$E_{V\text{Offset}}^{s\text{-GeSn}/r\text{-SiGeSn}} = E_{V\text{Offset}}^{r\text{-GeSn}/r\text{-SiGeSn}} + \max(\Delta E_{LH}^{s\text{-GeSn}}, \Delta E_{HH}^{s\text{-GeSn}}) \quad (5a)$$

$$\Delta E_{LH/HH}^{s\text{-GeSn}} = E_{LH/HH}^{s\text{-GeSn}} - E_{LH/HH}^{r\text{-GeSn}} \quad (5b)$$

The  $\Delta E_{LH}^{s\text{-GeSn}}$ , defined by Eq. (5b), is given in Table III. The  $\Delta E_{HH}^{s\text{-GeSn}}$  can be calculated from  $\Delta E_{LH}^{s\text{-GeSn}}$  and  $E_{HH}^\Gamma - E_{LH}^\Gamma$  in Table III. The band alignments of the remaining bands and CB-valleys can be obtained by adding the band energies calculated using the regression coefficients in Tables III and IV.

The EPM was used to obtain the band structure quantities for the BTBT model for the 3D simulation of a

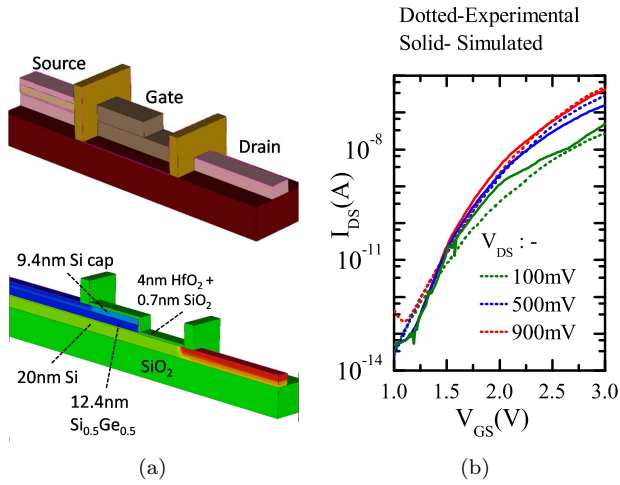


FIG. 5. (a) Device structure and vertical cross-section of the  $\text{Si}_{0.5}\text{Ge}_{0.5}/\text{Si}$  heterojunction nanowire-TFET simulated in 3D. (b) Comparison of simulated and experimental  $I_{\text{DS}}-V_{\text{GS}}$  characteristics. The parameters for fully relaxed SiGe layer on Si are used in the simulations (The figure is reprinted from Ref. 32 with permission. ©2014, IEEE publisher).

$\text{Si}_{0.5}\text{Ge}_{0.5}/\text{Si}$  hetero-structure TFET<sup>27</sup> with the device simulator S-Device<sup>28</sup>. The TFET has the form of a lateral nanowire etched from Si-cap/p++ $\text{Si}_{0.5}\text{Ge}_{0.5}/\text{n-Si}$  hetero-structures grown over  $\text{SiO}_2$ . Etching the nanowires down to Si at one end results in a step-like structure as shown in Fig. 5(a). The gate-stack contains a 4 nm thick  $\text{HfO}_2$  layer in addition to a  $\sim 7 \text{ \AA}$  native oxide (total Effective Oxide Thickness (EOT) =  $\sim 1.4 \text{ nm}$ ). The “dynamic non-local path BTBT model” and the Shockley-Read-Hall (SRH) generation-recombination model were employed in the simulations. The major contribution to the BTBT current comes from under-the-gate tunneling (“line tunneling”) in the SiGe layer along the vertical side-walls which necessitates 3D simulations. The simulated  $I_{\text{D}}-V_{\text{G}}$  characteristics of the device are in good agreement with the experimental  $I_{\text{D}}-V_{\text{G}}$  curves<sup>32</sup> (Fig. 5(b)) after adjusting the gate work function (i.e. increasing it from 4.25 eV to 5.1 eV). A large shift in the work function suggests quantization in the channel region which results in delayed turn-on. The slight underestimation of  $I_{\text{D}}$  at low  $V_{\text{G}}$  in the simulation is attributed to trap-assisted tunneling due to the defects present both at the SiGe/Si as well as the  $\text{HfO}_2/\text{SiGe}$  interface (not modeled). In this way, the device simulations yield a reasonable match with the experiments when the band structure quantities obtained from the EPM calculations described above are used as inputs to the BTBT model.

S. Sant would like to thank F. O. Heinz of Synopsys

LLC, Zurich, for useful discussions. Funding from the European Community’s Seventh Frame-work Programme under grant agreement No. 619509 (Project E<sup>2</sup>SWITCH) is acknowledged.

- <sup>1</sup>S. Gupta, B. Magyari-Köpe, Y. Nishi, and K. C. Saraswat, *J. Appl. Phys.* **113**, 073707 (2013).
- <sup>2</sup>P. Moontragoon, Z. Ikonc, and P. Harrison, *Semicond. Sci. Technol.* **22**, 742 (2007).
- <sup>3</sup>J. Kouvetakis, J. Menendez, and A.V.G. Chizmeshya, *Annu. Rev. Mater. Res.* **36** 497 (2006).
- <sup>4</sup>A. M. Ionescu, H. Riel, *Nature* **479**, 329 (2011).
- <sup>5</sup>S. Wirths, A. T. Tiedemann, Z. Ikonc, P. Harrison, B. Hollander, T. Stoica, G. Mussler, M. Myronov, J. M. Hartmann, D. Grützmacher, D. Buca, and S. Mantl, *Appl. Phys. Lett.* **102**, 192103 (2013).
- <sup>6</sup>Synopsys Inc., Sentaurus Device Monte Carlo User Guide, Version 2013.03, Mountain View, California, (2013).
- <sup>7</sup>J. R. Chelikowsky and M. L. Cohen, *Phys. Rev. B* **14**, 556 (1976).
- <sup>8</sup>S. Sant, S. Lodha, U. Ganguly, S. Mahapatra, F. O. Heinz, L. Smith, V. Moroz, and S. Ganguly, *J. Appl. Phys.* **113**, 033708 (2013).
- <sup>9</sup>P. Aella, C. Cook, J. Tolle, S. Zollner, A. V. G. Chizmeshya, and J. Kouvetakis, *Appl. Phys. Lett.* **84**, 888 (2004).
- <sup>10</sup>*Semiconductors: Group IV Elements and III-V Compounds*, edited by O. Madelung (Springer, New York, 1991).
- <sup>11</sup>G. Grzybowski, R. T. Beeler, L. Jiang, D. J. Smith, J. Kouvetakis, and J. Menendez, *Appl. Phys. Lett.* **101**, 072105 (2012).
- <sup>12</sup>R. Chen, H. Lin, Y. Huo, C. Hitzman, T. I. Kamins, and J. Harris, *Appl. Phys. Lett.* **99**, 181125 (2011).
- <sup>13</sup>J. Mathews, R. T. Beeler, J. Tolle, C. Xu, R. Roucka, J. Kouvetakis, and J. Menendez, *Appl. Phys. Lett.* **97**, 221912 (2010).
- <sup>14</sup>G. He, H. A. Atwater, *Phys. Rev. Lett.* **79**, 1937 (1997).
- <sup>15</sup>A. Tonkikh, C. Eisenschmidt, V. G. Talalaev, N. D. Zakharov, J. Schilling, G. Schmidt, and P. Werner, *Appl. Phys. Lett.* **103**, 032106 (2013).
- <sup>16</sup>V. D’Costa, Y.-Y. Fang, J. Tolle, J. Kouvetakis, and J. Menendez, *Phys. Rev. Lett.* **102**(10), 107403 (2009).
- <sup>17</sup>L. Jiang, C. Xu, J. D. Gallagher, R. Favaro, T. Aoki, J. Menendez, and J. Kouvetakis, *Chem. Mater.* **26**, 2522 (2014).
- <sup>18</sup>Y. P. Varshni, *Physica* **34**, 149 (1967).
- <sup>19</sup>V. D’Costa, C. Cook, A. Birdwell, C. L. Littler, M. Canonico, S. Zollner, J. Kouvetakis, and J. Menendez, *Phys. Rev. B* **73**, 125207 (2006).
- <sup>20</sup>P. Guevara, A. Rodriguez, H. Navarro-Contreras, and M. Vidal, *Appl. Phys. Lett.* **91**, 161909 (2007).
- <sup>21</sup>H. Lin, R. Chen, W. Lu, Y. Huo, T. Kamins, and J. Harris, *Appl. Phys. Lett.* **100**, 102109 (2012).
- <sup>22</sup>C. Eckhardt, K. Hummer, G. Kresse, *Phys. Rev. B* **89**, 165201 (2014).
- <sup>23</sup>M. Luisier and G. Klimeck, *J. Appl. Phys.* **107**, 084507 (2010).
- <sup>24</sup>M. V. Fischetti and S. E. Laux, *J. Appl. Phys.* **80**, 2234 (1996).
- <sup>25</sup>P. Moontragoon, R. A. Soref, and Z. Ikonc, *J. Appl. Phys.* **112**, 073106 (2012).
- <sup>26</sup>M. Jaros, *Phys. Rev. B* **37**, 7112 (1988).
- <sup>27</sup>S. Richter, S. Blaesus, L. Knoll, S. Trelenkamp, A. Schäfer, J. M. Hartmann, Q. T. Zhao, S. Mantl, *IEEE ULIS’13*, p.25 (2013).
- <sup>28</sup>Synopsys Inc., Sentaurus Device User Guide, Version 2013.03, Mountain View, California, (2013).
- <sup>29</sup>E. O. Kane, *J. Phys. Chem. Solids* **12**, 181 (1959).
- <sup>30</sup>E. O. Kane, *J. Appl. Phys.* **32**, 83 (1961).
- <sup>31</sup>O. Penzin, G. Paasch, F. O. Heinz, L. Smith, *IEEE Trans. on Elec. Dev.* **58**, p. 1614 (2011).
- <sup>32</sup>S. Sant, Q. Zhao, D. Buca, S. Mantl, and A. Schenk, *IEEE SISPAD’14*, 125 (2014) [©2014, IEEE publisher].